

### RESEARCH ARTICLE

# Dynamic response of Akcakoca RCC Dam including galleries

Muhammet Ensar Yiğit<sup>1\*</sup>, Murat Emre Kartal<sup>2</sup>, Fethi Şermet<sup>3</sup>, Emin Hökelekli<sup>4</sup>

- <sup>1</sup> Manisa Celal Bayar University, Faculty of Engineering, Civil Engineering Department, Manisa, Türkiye
- <sup>2</sup> İzmir Demokrasi University, Faculty of Engineering, Civil Engineering Department, İzmir, Türkiye
- <sup>3</sup> Iğdır University, Faculty of Engineering, Civil Engineering Department, Iğdır, Türkiye
- <sup>4</sup> Bartın University, Faculty of Engineering, Civil Engineering Department, Bartın, Türkiye

### **Article History**

Received 21 November 2023 Accepted 27 May 2024

### Keywords

RCC dam
Eulerian-Lagrangian coupled analysis
Fluid mechanics
Hydromechanics
Structure dynamics
Numerical modeling

### **Abstract**

Dams are structures that demand a significant amount of concrete, making them costly constructions. Hence, various alternative methods are employed for dam construction, one of which is the use of Roller Compacted Concrete (RCC). This is a case study, which focuses on examining the behavior of RCC dams with and without galleries under seismic excitations, considering the Akçakoca RCC dam in Düzce Province. The seismic ground motion data from the 1999 Düzce earthquake were utilized. The impact of galleries inside the concrete dams was investigated through stress and displacement, considering both empty and full reservoir conditions. The Eulerian-Lagrangian coupled (CEL) approach was employed for two-dimensional fluid finite elements. This study revealed that reservoir water and galleries have a notable influence on the behavior of dams under seismic forces. In cases with reservoirs and galleries, stress and displacement values increased, and critical changes in stresses were observed around gallery areas. Therefore, careful design considerations are essential for dams with galleries under significant seismic forces.

#### 1. Introduction

The roller-compacted concrete dam method involves enriching traditional granular fill or mass concrete aggregates with cement. These enriched materials are placed and compacted in single or multiple layers using conventional construction equipment, forming a dam. The concrete used in such dams is referred to as Roller Compacted Concrete (RCC). RCC stands out from regular concrete due to its dense consistency and appearance, resembling sand and gravel materials. Due to its solid state, it can only be compacted using vibrators. The first RCC dam was constructed in 1981 at the Shimajigawa Dam in Japan. In Turkey, the RCC method was initially applied in the foundation cutoffs of the Karakaya Dam and later in specific structures of the Atatürk, Sır, Berke, and Kürtün (foundation cutoff) dams. Additionally, RCC was used in the design of the body structures of the Cindere Dam and Hydroelectric Power Plant, Çine Dam and Hydroelectric Power Plant, as well as the Akköy I Dam and Hydroelectric Power Plant, constructed within the borders of Kürtün District in Gümüşhane Province [1].

<sup>\*</sup> Corresponding author (ensar.yigit@cbu.edu.tr)

In recent research studies, Noorzaei et al. [2] delved into the thermal behavior of Roller Compacted Concrete (RCC) dams, shedding light on their thermal characteristics. Jaafar et al. [3] underscored the pivotal role of thermal analyses in roller-compacted concrete dams, emphasizing the need for optimizing concrete pouring processes based on temperature zones. Omidi et al. [4] employed a plastic damage model to simulate irreversible damage occurring during the concrete failure process, providing insights into the structural integrity of the dams. Huang et al. [5] highlighted the influence of rising water levels on seepage rates and dynamic effects, contributing to a comprehensive understanding of dam behavior under varying hydrological conditions. Araujo et al. [6] proposed an innovative method that takes into account the complex interaction between dam, reservoir, and foundation, providing probabilistic solutions crucial for concrete gravity dams. Yilmazturk et al. [7] conducted seismic analyses, considering the intricate interaction between dam, reservoir, and ground, providing valuable insights into the seismic response of high Roller Compacted Concrete (RCC) gravity dams. Liang et al. [8] developed robust reliability and probability theories to assess sliding conditions in layered fill dams and slopes, revealing significant findings related to dam stability. Xiong et al. [9] delved into the seismic behavior of dams during high-magnitude earthquakes, exploring the influence of diverse material properties on dam responses under extreme seismic forces. Cheng et al. [10] employed modal analysis techniques to monitor dam safety, offering recommendations on modal parameter identification methods tailored for concrete gravity dams, crucial for ongoing structural evaluations. Zhong et al. [11] highlighted crucial factors such as cracks and material property collapse that significantly impact the stability of high concrete dams under strong seismic events, providing essential insights for dam safety assessments, Additionally, Li et al. [12] conducted meticulous examinations on RCC dams, focusing on various waterproof concrete layers in tension and leakage conditions on the upstream face. Their findings emphasized the imperative need for impermeability in the top layer to ensure long-term dam integrity.

Various studies have been conducted using Finite Element Analysis (FEM) techniques to evaluate the seismic performance of Roller Compacted Concrete (RCC) dams. Sharma et al. [13] applied FEM for nonlinear dynamic failure analysis in a concrete gravity dam. Wang et al. [14] conducted a three-dimensional dynamic nonlinear finite element analysis, revealing significant damage concentrated in the middle monoliths of the riverbed in seismic scenarios. Calayir and Karaton [15] utilized FEM for two-dimensional seismic analyses of the Koyna gravity dam, incorporating 1967 Koyna earthquake records for dam-reservoir interaction simulations. Bayraktar et al. [16] explored the impact of reservoir length on the seismic performance of gravity dams against near and far fault ground motions. Kartal [17] studied the seismic response of 3D roller-compacted concrete dams using FEM to observe the behavior of SSB dams. Huang [18] developed a numerical framework for seismic failure analysis in dam-reservoir-rock-soil interactive systems. Kartal et al. [19] investigated the seismic response of 2D roller-compacted concrete dams under different reservoir lengths. Zhuo et al. [20] conducted a numerical study on the seismic behavior of Shapai SSB arch dams. Mejia et al. [21] discussed evaluating dam improvement alternatives, design criteria, and seismic retrofitting using detailed analysis. Wang et al. [22] introduced the Extended Finite Element Method (XFEM) to describe crack propagation in concrete gravity dams under seismic loads. Hariri et al. [23] examined the impact of various earthquake accelerations on dam-reservoir-ground models using the Lagrangian-Eulerian approach, analyzing near-fault and far-fault earthquakes' influence on crack formation. Jiang et al. [24] investigated crack behavior in concrete gravity dams using the finite element method. These studies collectively contribute to our understanding of RCC dam seismic responses and inform critical aspects of their design and analysis.

Hariri et al. [25] the seismic response of gravity dams is analyzed using random field theory, incorporating uncertainty in material properties. The research focuses on the Koyna Gravity Dam, employing numerical simulations where concrete properties like modulus of elasticity, mass density, and tensile strength are treated as random fields. The study explores various factors such as correlation length, material

distribution, ground motion intensity, and dam class. The results highlight the significance of considering concrete heterogeneity in seismic performance evaluation for structural assessment and risk analysis. For dams exceeding a height of 30 meters, the presence of galleries is essential for studying and observing dam behavior. Additionally, galleries are important for creating drainage and injection holes in the foundation and establishing areas for leakage drainage. It is crucial to position the galleries in a way that does not obstruct dam construction [26].

In the numerical analysis of roller compacted concrete (RCC) dams under static and dynamic loads, the dam body is traditionally considered solid without considering the presence of galleries inside. However, galleries usually exist within the body, and it is expected that stress accumulations occur in these areas. To accurately determine these stress accumulations and assess whether they pose a risk, a finite element mesh refinement may be performed around the gallery. This study aims to compare the maximum stresses in two-dimensional numerical models considering galleries or not. In this study, two-dimensional (2D) finite element models of RCC dams were designed, taking galleries into account, using the actual coordinate data of the dam. The mechanical material properties of the rock foundation and concrete used in the design, considering the geological conditions of the dam region, such as modulus of elasticity and Poisson's ratio, into the ABAQUS software. The presented study focused on the Akçakoca RCC dam located in the Düzce province.

## Formulation of Eulerian-Lagrangian coupled approach for dam-reservoir-foundation interaction

The Eulerian-Lagrangian Coupled Approach provides a robust framework to investigate the intricate interactions within dams, considering both the broader spatial context and the behavior of individual elements. This comprehensive analysis aids in making informed decisions regarding dam safety, structural integrity, and risk assessment. In the context of fluid dynamics and continuum mechanics, the Eulerian and Lagrangian descriptions are two fundamental approaches used to analyze the motion and behavior of materials.

In the Eulerian description, the focus is on specific points or regions in space, and equations are formulated based on the properties observed at these fixed spatial locations. The Eulerian approach tracks how properties (such as velocity, pressure, or temperature) change over time at these fixed points. In contrast, the Lagrangian description follows the motion of individual particles or elements of a material. Here, each particle is tracked as it moves through space and time. The equations are formulated based on the properties associated with each specific particle, considering its position and velocity at any given time.

The connection between material and spatial time derivatives can be articulated in the following manner:

$$\frac{D\Phi}{Dt} = \frac{\partial\Phi}{\partial t} + v.\left(\nabla\Phi\right) \tag{1}$$

where  $\Phi$  represents the arbitrary solution variable, v denotes the material velocity.  $D\Phi/Dt$  represents the material time derivative, and  $\partial\Phi/\partial t$  represents the spatial time derivative. The conservation equations for mass, momentum, and energy, initially formulated in the Lagrangian framework, are converted into Eulerian conservation equations (involving spatial derivatives) as detailed in the provided reference. [27].

$$\frac{\partial \rho}{\partial t} + v.(\nabla \cdot \rho) + \rho \nabla \cdot v = 0 \tag{2}$$

$$\frac{\partial v}{\partial t} + v.(\nabla \cdot v) = \frac{1}{\rho}(\nabla \cdot \sigma) + b \tag{3}$$

$$\frac{\partial e}{\partial t} + v. (\nabla e) = \sigma: D \tag{4}$$

where  $\rho$  represents density,  $\sigma$  denotes the Cauchy stress, b is the vector of body forces, e stands for strain energy, and D represents velocity strain. The equations in the Eulerian framework (Eqs. 2 to 4) can be reformulated in conservative formats as follows [28]:

$$\frac{\partial \rho}{\partial t} + \nabla \cdot (\rho v) = 0 \tag{5}$$

$$\frac{\partial \rho v}{\partial t} + \nabla \cdot (\rho v \otimes v) = \nabla \cdot \sigma + \rho b \tag{6}$$

$$\frac{\partial e}{\partial t} + \nabla \cdot (ev) = \sigma : D \tag{7}$$

The Eulerian governing equations (5) to (7) have a general form:

$$\frac{\partial \phi}{\partial t} + \nabla \cdot \varphi = S \tag{8}$$

where  $\phi$  represents the flux function, and S represents the source term. Eq. (8) is divided into two equations and solved sequentially using operator splitting, as described in reference.

$$\frac{\partial \phi}{\partial t} = S \tag{9}$$

$$\frac{\partial \phi}{\partial t} + \nabla \cdot \varphi = 0 \tag{10}$$

where Eq. (9) includes the source term, which signifies the Lagrangian step, whereas Eq. (10) incorporates the convective term, symbolizing the Eulerian step. A visual depiction of this split operator is presented in Fig. 1.

To solve Eq. (10), the distorted mesh from the Lagrangian step is moved to the fixed Eulerian mesh, and the volume of material transferred between neighboring elements is computed. The Lagrangian solution parameters like mass, stress, and energy are modified to accommodate the material flow between adjacent elements. The principle of virtual work is employed in the Lagrangian step as described in reference [29].

$$\int_{v} \rho a. \, \delta u dv + \int_{v} \sigma : \delta \varepsilon dV = \int_{S} t. \, \delta u dS + \int_{v} \rho b. \, \delta u dV \tag{11}$$

In the Lagrangian step, the updated Lagrangian formulation is suitable because it corresponds to the current configuration in the Eulerian approach, aligning with the reference configuration at time t. However, predicting the configuration of the body at  $t+\Delta t$ , as described in Eq. (11), is generally challenging. This prediction includes unknown factors such as the volume of integration and density, which both depend on the deformations of the body. Moreover, determining the Cauchy stress at  $t+\Delta t$  is not straightforward, as it cannot be obtained by merely adding the stress increment to the Cauchy stress at t. This complexity arises because the components of the Cauchy stress tensor change when the material undergoes rigid body rotations. To handle these challenges practically, alternative strain and stress measures come into play, such as the Green-Lagrange strain tensor and the second Piola-Kirchoff stress tensor. These measures are employed in the principle of virtual displacements (Eq. 11) to accurately represent the behavior of the material under deformation [30].

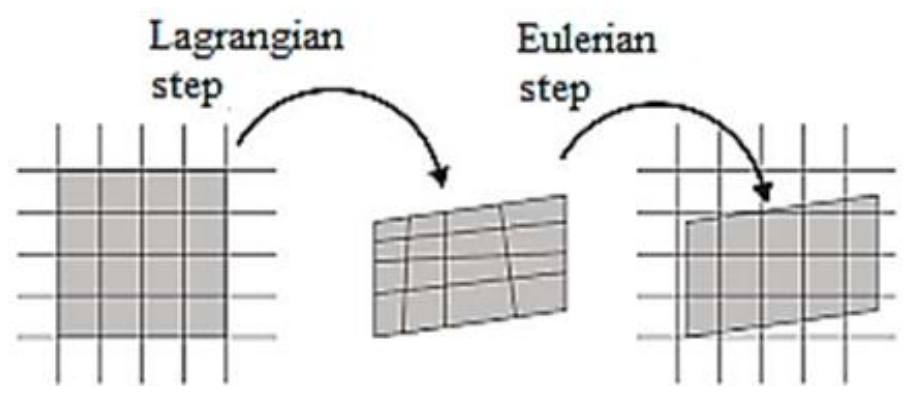


Fig. 1. The use of the split operator in the CEL formulation [34]

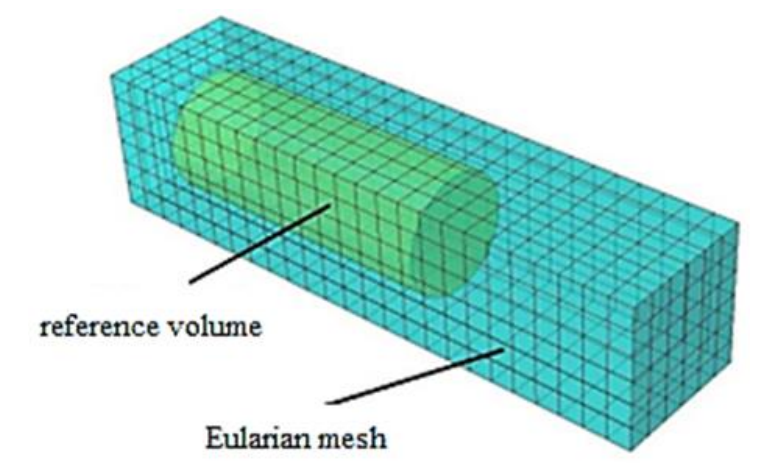


Fig. 2. Volume fraction parameter estimation in computational analysis [34]

In the context of simulations involving the Eulerian mesh, understanding the presence or distribution of materials is crucial. To achieve this, a parameter called the volume fraction (VF) is introduced [31]. This parameter essentially represents the ratio of the volume occupied by materials within the Eulerian mesh to the total volume available. To begin this calculation, researchers need to establish the initial volume fraction, which essentially means determining how much space the materials occupy within the fixed, predefined Eulerian mesh. This initial volume fraction is a vital reference point, allowing researchers to assess the distribution and presence of materials accurately. Fig. 2 likely provides a visual representation of this reference volume, helping researchers understand the initial configuration within the Eulerian mesh.

#### 3. Mathematical model of Akcakoca RCC Dam

#### 3.1. Akcakoca Dam

The Akcakoca dam, situated around 17 km north of Düzce, was built in 2016 by the State Hydraulic Works of Türkiye. It is located at the mouth of Akcakoca and was designed as a roller-compacted concrete dam (Fig. 3). Primarily utilized for irrigation, the dam's crest spans 150 meters in length and 8 meters in width. The dam reaches a maximum height of 66 meters, and the reservoir's water level is maintained at a maximum of 62 meters.



Fig. 3. Akçakoca Dam

#### 3.2. Characteristics of materials used in Akcakoca RCC Dam

The 2D finite element simulation of the Akcakoca dam incorporates a single-layered foundation made of gneiss rock. Details of the material properties for both the dam body and the foundation of the Akcakoca roller compacted concrete dam can be found in Table 1.

#### 3.3. Finite element models of Akcakoca Dam

This study utilizes a two-dimensional finite element model (FEM) for the Akcakoca RCC dam. In this model, the dam's height is denoted as 'H'. The foundation rock extends 'H' units in both the downstream river direction and gravity direction. Furthermore, the foundation rock and reservoir water model extend '3H' units in the upstream direction (Fig. 4.). Wilson and Khalvati (1983) introduced an innovative Lagrangian approach designed to remove specific zero energy modes, resulting in a fluid element displaying optimal behavior. Within the solid elements, the dam body (C3D8) is structured with a 2×2 integration point, the foundation rock (C3D8) also employs a 2×2 pattern, and the fluid element (EC3D8) incorporates 2×2 integration points.

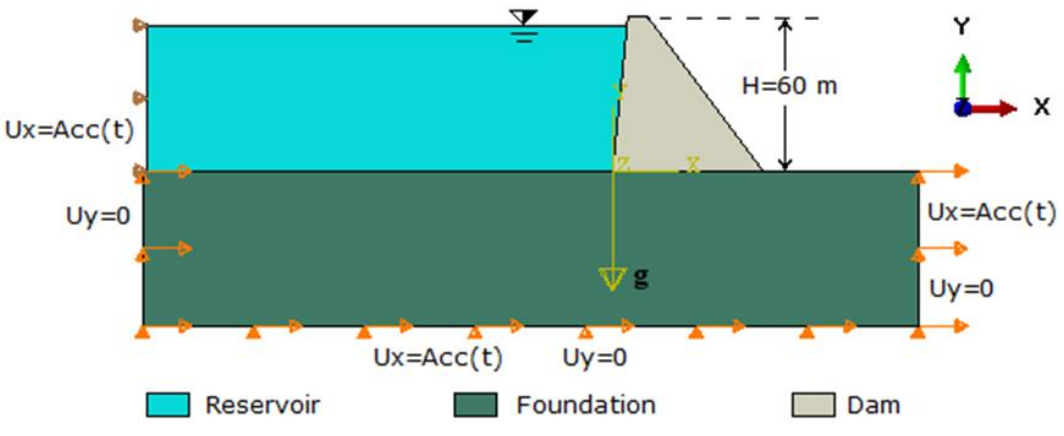


Fig. 4. Finite element model of dam

	•		
Element	Modulus of Elasticity (GPa)	Poisson's ratio	Mass density (kg/m³)
Concrete (Dam Body)	28	0.2	2500
Gneiss	18	0.15	2800
Water	2.2	-	1000

Table 1. Material properties of Akcakoca roller compacted concrete dam

In this research, we simulated the behavior of the RCC dam with and without galleries to assess the impact of galleries on the dam's response to seismic activity. Using ABAQUS software, we created a two-dimensional finite element model specifically focusing on the critical section of the Akcakoca RCC dam. By varying the dam height, we calculated the maximum tensile and compressive stresses. Subsequently, we analyzed the maximum principal tensile and compressive stresses experienced by the upstream side of the dam body during an earthquake. These stress components were visualized through contour diagrams. Four distinct scenarios were investigated to identify the most vulnerable conditions of the dam in this study.

- a) The first case involves an empty reservoir and galleries are excluded from the dam body. This model has a total of 6092 nodal points and 2844 elements (Fig. 5).
- b) The second case involves a full reservoir and galleries are excluded from the dam body. This model has a total of 13542 nodal points and 6427 elements (Fig. 6).
- c) The third case involves an empty reservoir and considering galleries in the dam. This model has a total of 6230 nodal points and 2907 elements (Fig. 7).
- d) The fourth case involves a full reservoir and considering galleries in the dam. This model has a total of 6592 elements and 13888 nodal points (Fig. 8).

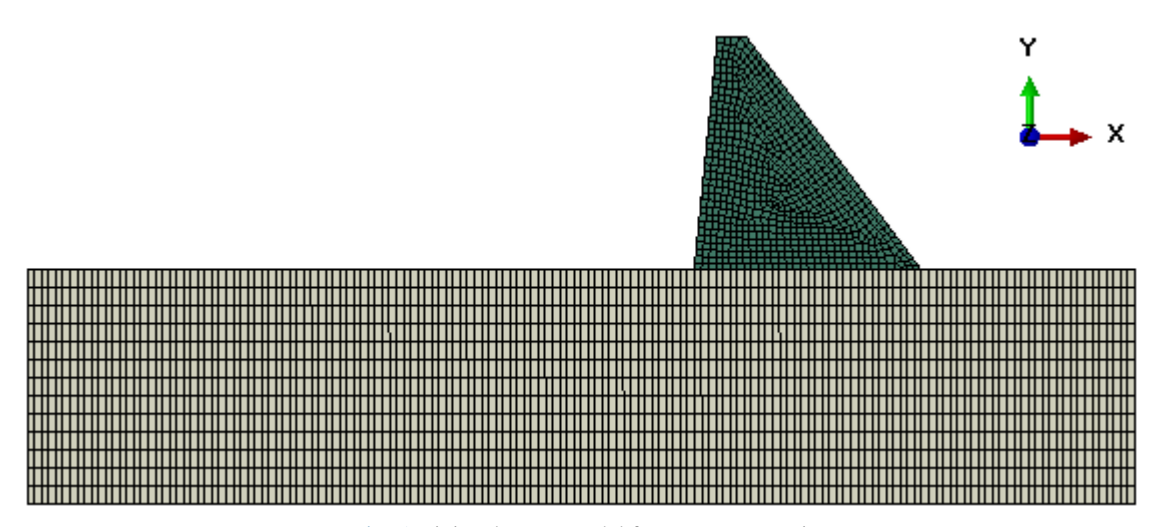


Fig. 5. Finite element model for empty reservoir

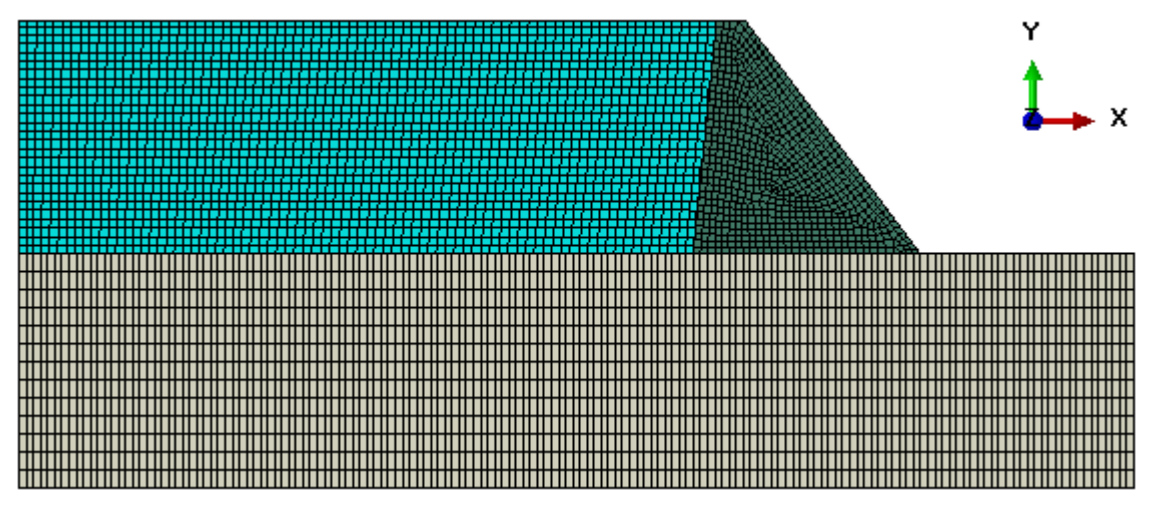


Fig. 6. Finite element model for full reservoir

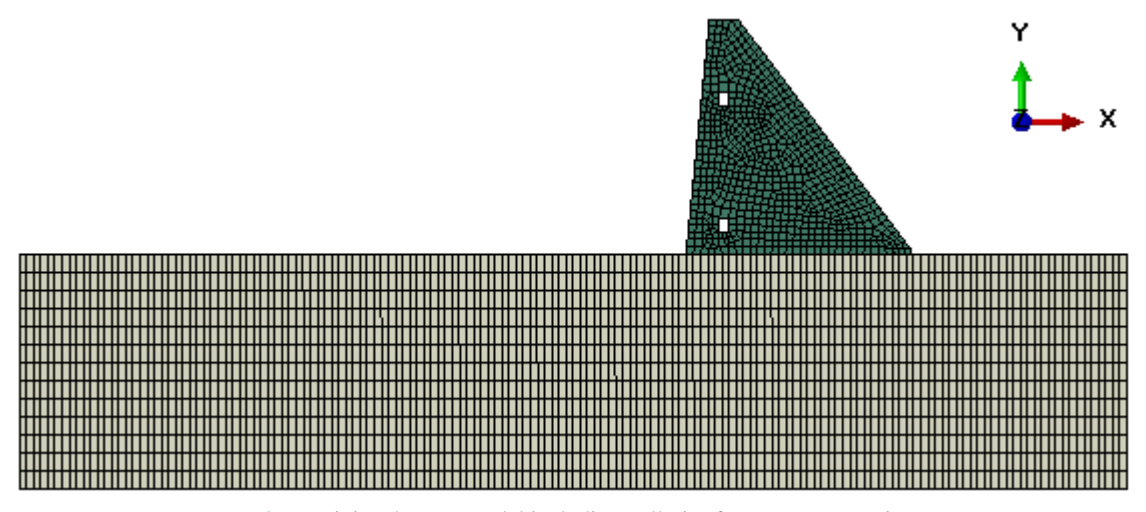


Fig. 7. Finite element model including galleries for empty reservoir

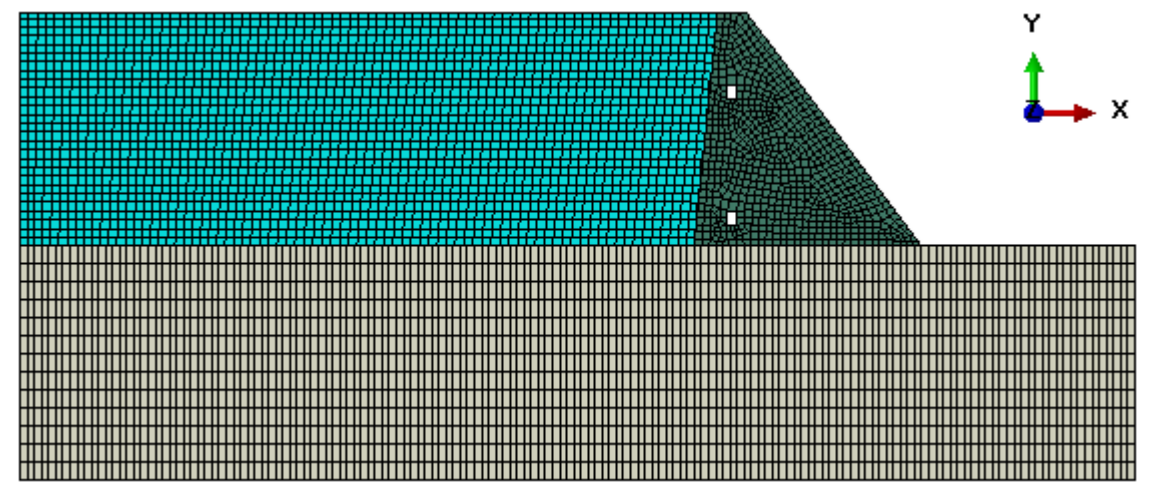


Fig. 8. Finite element model including galleries for full reservoir

#### 3.4. The seismic event that occurred in Düzce in 1999

The earthquake in Düzce, which struck on November 12, 1999, at 18:57 local time (16:57 UTC) with a moment magnitude of 7.2, resulted in significant damage, causing 845 fatalities and 4,948 injuries in Düzce, Türkiye. The earthquake's epicenter was located at coordinates 40.768, and 31.148, with a moment magnitude of 6.2 (Mb = 6.2, Ms = 7.4). The seismic moment was  $Mo = 4.5 \times 1019$  Nm, and the magnitude was Mw = 7.1 [33]. In this study, we utilized the north-south component of the 1999 Düzce accelerogram, as shown in Fig. 9.

### 3.5. Optimum mesh density choose

In numerical studies, achieving accurate results relies on creating a finite element mesh that suits the analysis requirements. To identify the optimal mesh, various finite element splitting models need to be analyzed and their outcomes compared. Particularly in areas where stress spikes occur abruptly, such as around galleries, the choice of finite element mesh significantly impacts stress values. Investigations were conducted using different discretizations to observe stress variations due to sudden section loss around the gallery. Fig. 10 illustrates the findings of this investigation, determining the optimal number of finite elements for the gallery perimeter based on numerical analysis results.

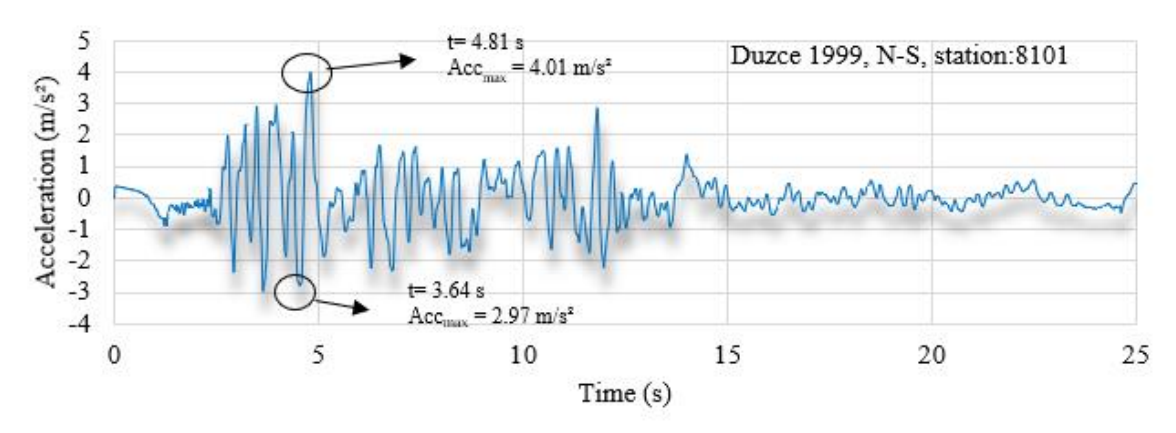


Fig. 9. 1999 Düzce N-S earthquake accelerogram

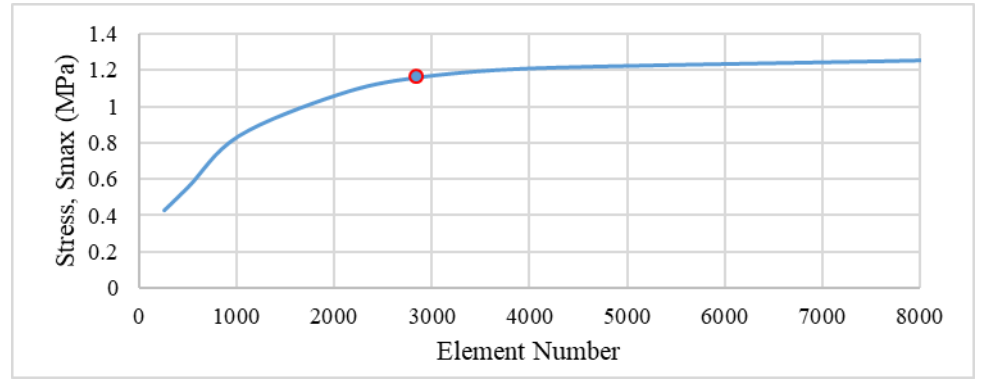


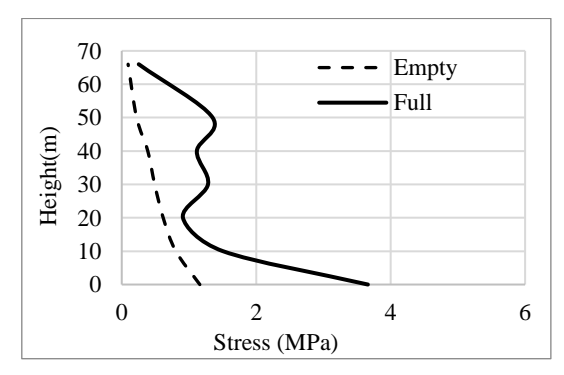
Fig. 10. Evaluation for optimum finite element mesh around upstream face thalweg

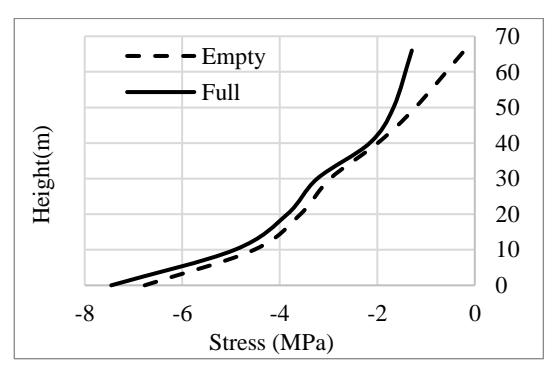
### 4. Dynamic analysis results

We investigated five different aspects due to the four cases as indicated preceding section. In the numerical solutions, we did not describe any friction elements between the dam body and foundation rock interface and considered welded contact as conventional modeling. First of all, we investigated the tensile stress change by height of the dam (Figs. 11-12). The second one is that horizontal displacement change is studied by the height of the dam (Figs. 13-14). Then, we researched the horizontal displacement changing by time at the top point of the crest (Figs. 15-16). The fourth one is the tensile and compressive stress change during the earthquake at the bottom point of the upstream side (Figs. 17-20). In this case, the contour diagrams for the most critical principal stresses are also shown (Figs. 21-24). Finally, the last one is the tensile and compressive stress change at the selected critical points around galleries inside the dam (Figs. 25-29). The contour diagrams for the most critical principal stresses around galleries are also shown (Figs. 30-33).

### 4.1. Stresses by height

The variation of tensile stresses with the dam height in both empty and full conditions of both the dam without and with a gallery is shown in Figs. 11 and 12, respectively. There was a significant increase in maximum tensile stresses in the dam with a gallery. In the case of the dam with a gallery being empty, the tensile stress was 3.66 MPa (Fig. 11a), while an increase occurred in the tensile stress when the dam was full, reaching 4.11 MPa (Fig. 12a). However, the rise in compressive stress values was relatively minor (Fig. 11b, Fig. 12b).



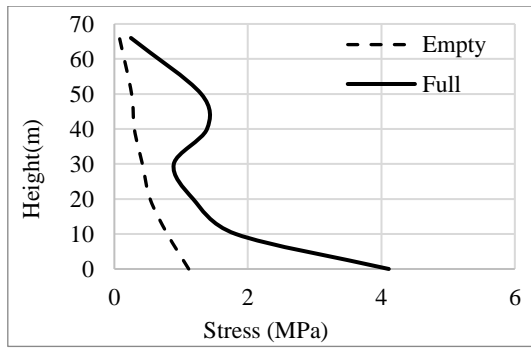


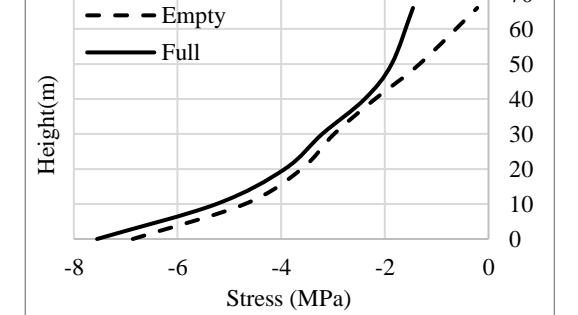
a) Maximum tensile principal stress

b) Minimum compressive principal stress

70

Fig. 11. Principal stress chancing by height without gallery condition





- a) Maximum tensile principal stress
- b) Minimum compressive principal stress

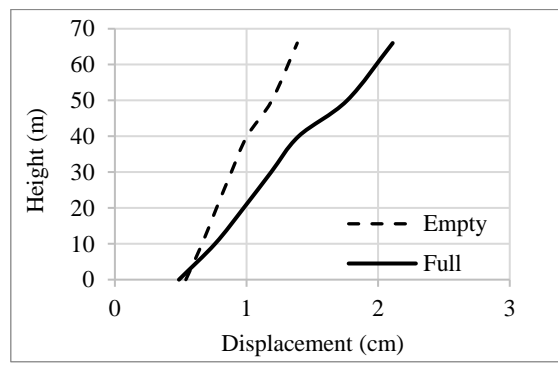
Fig. 12. Principal stress chancing by height including gallery condition

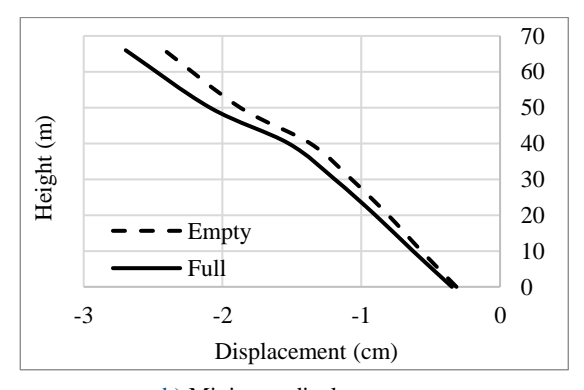
### 4.2. Displacements by height

In this section, Figs. 13 and 14 illustrate the changes in dam height concerning displacement under seismic excitations, considering different scenarios: empty and full reservoir, both with and without a gallery. There was an increase in displacements along the height in both scenarios. Significantly, displacement experiences a notable increase due to the hydrostatic pressure force in the full condition. At the peak, with the gallery filled, a displacement of 2.24 cm (Fig. 14b) was noted, whereas, without a gallery under similar full conditions, the displacement measured 2.11 cm (Fig. 13a). The inclusion of a gallery in the dam has resulted in increased displacements, irrespective of whether the dam reservoir is empty or full.

### 4.3. Displacements during earthquake

The displacement variations over time under earthquake effects for different dam conditions, including empty and full reservoir conditions, as well as with and without galleries, are illustrated in Figs. 15-16. Displacements in empty dams, with or without galleries, exhibited similarity, with minimal difference between the two scenarios. Nonetheless, in filled conditions, whether with or without galleries, the stresses observed over time were higher compared to those in empty dams, primarily due to the influence of water. When the dam is full, damping (the decrease in displacement over time) was relatively lower compared to empty scenarios, suggesting a slower reduction in displacement under the influence of earthquake forces.

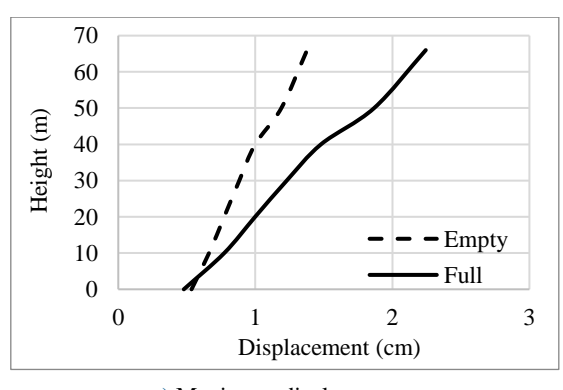


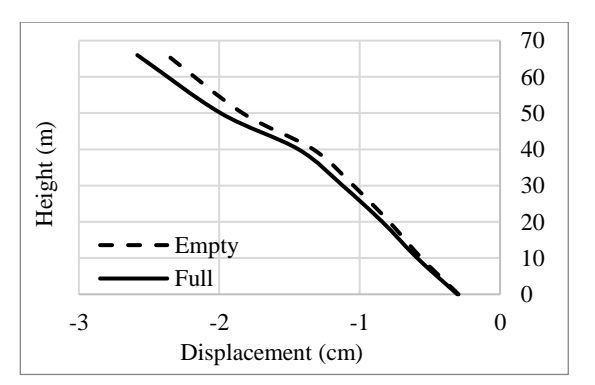


a) Maximum displacements

b) Minimum displacements

Fig. 13. Horizontal relative displacements chancing by height without gallery condition

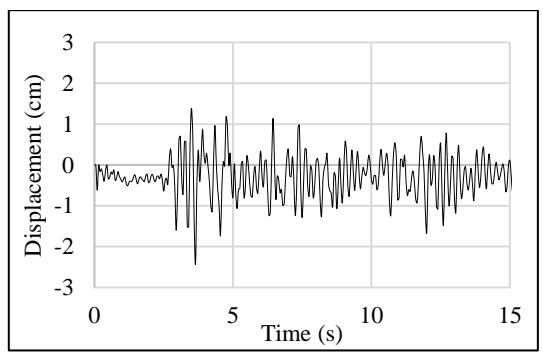


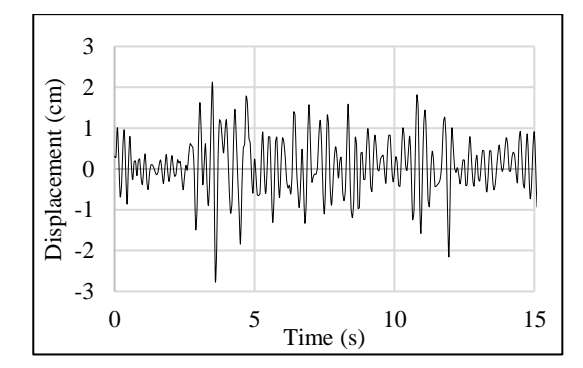


a) Maximum displacements

b) Minimum displacements

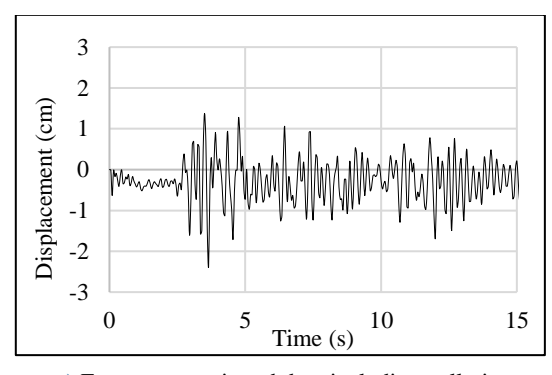
Fig. 14. Horizontal relative displacement chancing by height including gallery condition

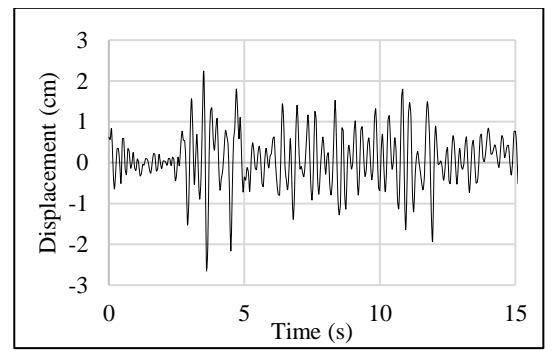




- a) Empty reservoir and dam without galleries
- b) Full reservoir and dam without galleries

Fig. 15. Horizontal displacement changes at crest during the earthquake without gallery model





- a) Empty reservoir and dam including galleries
- b) Full reservoir and dam including galleries

Fig. 16. Horizontal displacement changes at crest during earthquake including gallery model

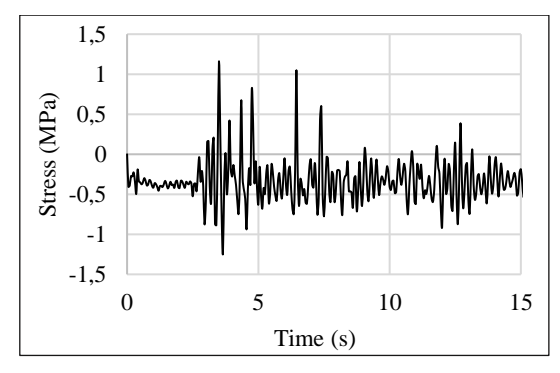
### 4.4. Stresses during earthquake

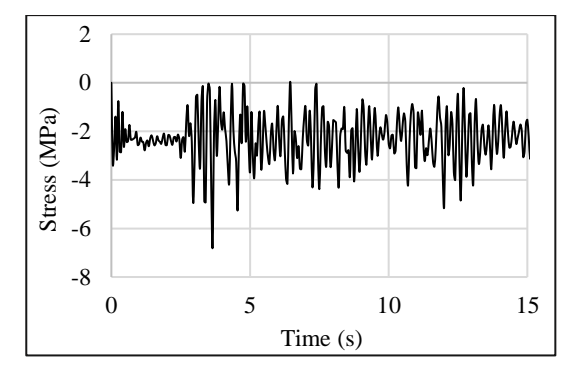
For the dam without galleries, stress-time graphs for the upstream thalweg under earthquake forces for both empty and full reservoir conditions are presented in Figs. 17 and 18, respectively. In the empty condition, the maximum principal tensile stress was 1.16 MPa, while in the full condition, it increased significantly to 3.50 MPa. Similarly, when the reservoir was empty the maximum principal compressive stress values measured at -6.77 MPa, and slightly decreased to -7.45 MPa when the reservoir was full. The stress-time graphs for the dam with a gallery, in both empty and full reservoir conditions, are respectively illustrated in Figs. 19 and 20. The maximum principal tensile stress in the empty state was 1.31 MPa, increasing to 4.11 MPa in the full state. The maximum principal compressive stress values were -6.86 MPa in the empty state, and they decreased slightly to -7.55 MPa in the full state. The analysis shows that the stress values in the full conditions are higher than in the empty condition, and the highest stress values occur in the full gallery dam model. The presence of water and gallery shows that it has a significant impact on the structural behavior of the dam under earthquake forces.

### 4.5. Principal stress distributions

The maximum and minimum principal stress distributions of empty and full dams without galleries are given in Figs. 21-22. In the empty state, the maximum and minimum principal stress values were 1.161 MPa and -6.77 MPa, respectively. In the full state, both stress values increased, reaching 3.661 MPa for the maximum principal stress and -7.456 MPa for the minimum principal stress. These elevated stress levels were notably concentrated at the corner points where the body and the head part of the structure meet (upstream face

thalweg). Fig. 23 and Fig. 24 represent the distributions of maximum principal stress and minimum principal stress in the dam under both empty and full conditions with a gallery, respectively. In the empty state, the maximum principal stress and minimum principal stress values were 1.114 MPa and -6.863 MPa, respectively. In the full state, these stress values increased to 4.112 MPa for the maximum principal stress and -7.552 MPa for the minimum principal stress. The areas experiencing the highest stresses were identified as the upstream face thalweg.

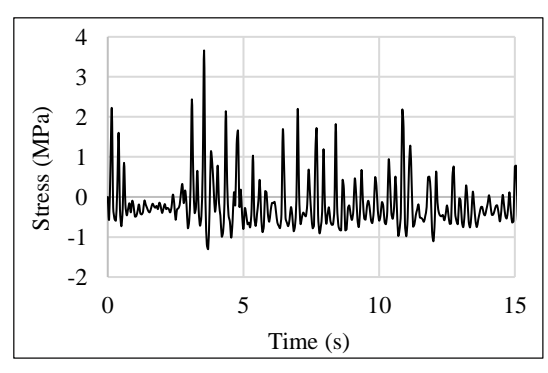


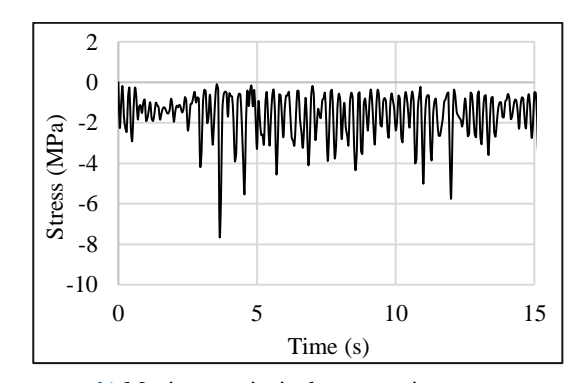


a) Maximum principal tensile stress

b) Maximum principal compressive stress

Fig. 17. Stress change at thalweg for empty reservoir condition during the earthquake without galleries

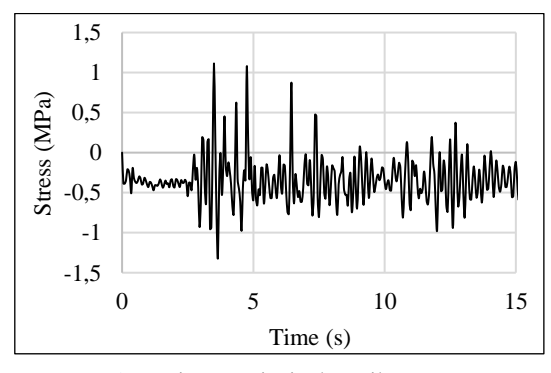


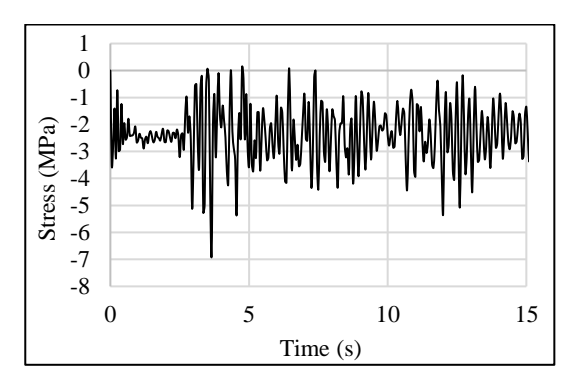


a) Maximum principal tensile stress

b) Maximum principal compressive stress

Fig. 18. Stress changing at thalweg for full reservoir condition during the earthquake without galleries

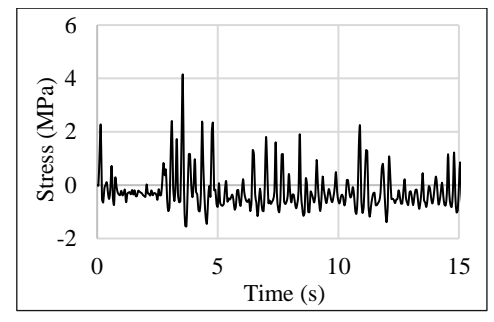


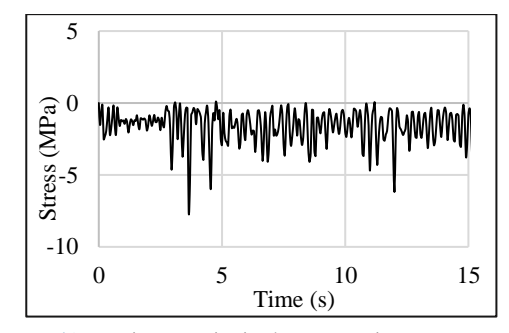


a) Maximum principal tensile stress

b) Maximum principal compressive stress

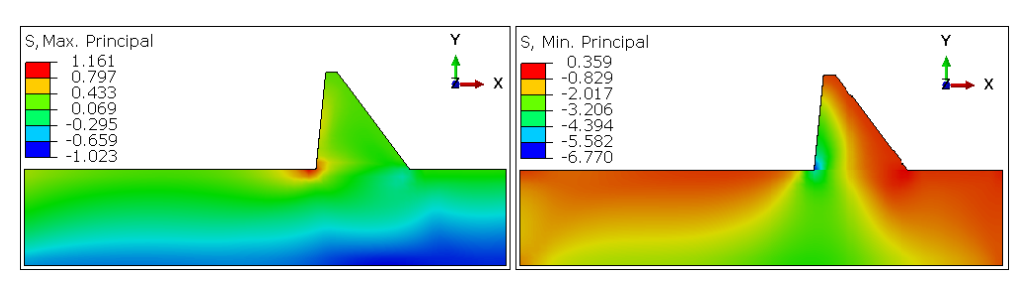
Fig. 19. Stress change at thalweg for empty reservoir condition during the earthquake including galleries





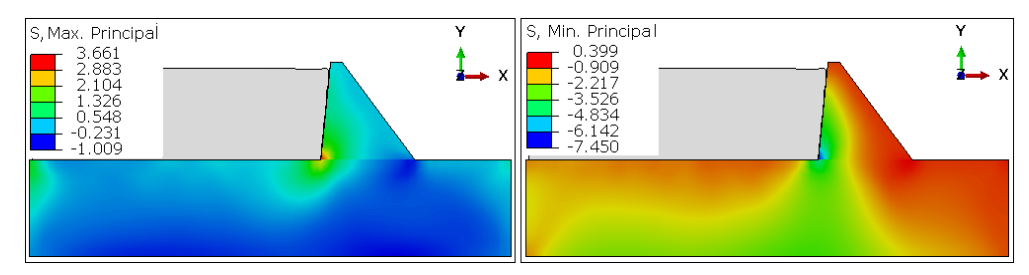
- a) Maximum principal tensile stress
- b) Maximum principal compressive stress

Fig. 20. Stress changing at thalweg for full reservoir condition during earthquake including galleries



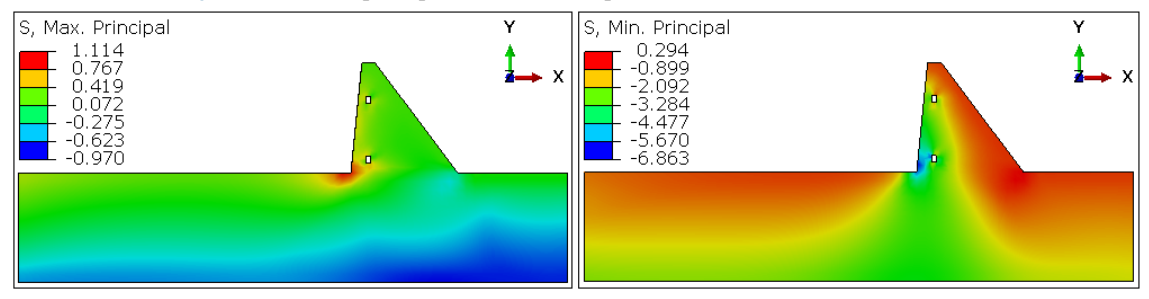
- a) t=3.50, max. principal stress 1.161 MPa
- b) t=3.65, min. principal stress = -6.770 MPa

Fig. 21. Maximum and minimum principal stresses at the upstream side in empty reservoir condition



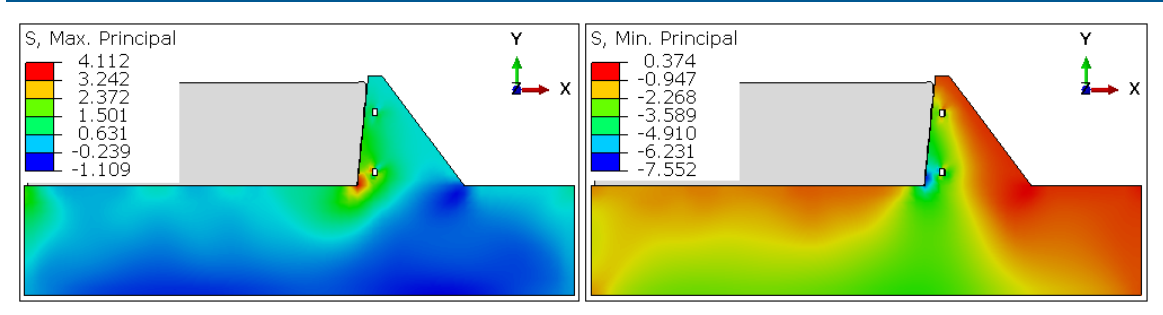
- a) t= 3.55 s, max principal stress= 3.661 MPa
- b) t= 3,65 s, min principal stress= -7.456 MPa

Fig. 22. Maximum principal stresses at the upstream side in full reservoir condition



- a) t= 3.50 s, max principal stress= 1.114 MPa
- b) t= 3,65 s, min principal stress= -6,863 MPa

Fig. 23. Maximum principal stresses at the upstream side in the empty reservoir including gallery conditions



a) t= 3.55 s, max principal stress= 4.112 MPa

b) t= 3,65 s, min principal stress= -7,552 MPa

Fig. 24. Maximum principal stresses at the upstream side in the full reservoir including gallery conditions

This analysis demonstrates that the stress levels are significantly higher in the gallery and filled dam models, emphasizing the importance of considering these factors in understanding the structural behavior and stress distribution in the dam under different states.

#### 4.6. Stresses around galleries

Details of the galleries and the mesh model are given in Fig. 25. When the dam is empty, the stress time graph of the point around the upper gallery is given in Fig. 26 and the point around the lower gallery is given in Fig. 27. If the dam is full, the stress time graph of the point around the upper gallery is given in Fig. 28 and the point around the lower gallery is given in Fig. 29. In Fig. 30, the top gallery node 889 experienced maximum tensile stress of 0.276 MPa at 3.30 seconds when the dam was empty. Simultaneously, the minimum compressive stress reached -2.317 MPa at 3.65 seconds. In Fig. 32, under full conditions, the maximum tensile stress rose substantially to 0.965 MPa, while the minimum compressive stress reached -2.613 MPa. This increase in maximum tensile stress in the full condition was primarily attributed to the hydrostatic pressure exerted by the water. The stress values observed in both empty and full states align with the stress-time graphs presented in Figs. 26 and 28. These figures collectively demonstrate the variation of stresses over time and provide a clear comparison between the stress states of the dam under different conditions.

In Fig. 31, when the dam was empty, the maximum tensile stress and minimum compressive stress values at the bottom gallery node 878 were 0.448 MPa and -4.171 MPa, respectively. In Fig. 33, under full conditions, the maximum tensile stress and minimum compressive stress values at the bottom gallery node 878 increased significantly to 2.105 MPa and -4.443 MPa, respectively. This indicates an approximately 5-fold increase in the maximum tensile stress value when the dam is in a full state. The stress values observed in the galleries, as depicted in Figs. 31-33, align with the stress-time graphs presented in Figs. 27-29. These figures collectively illustrate the variation of stresses over time and provide a clear comparison between the stress states of the dam in the presence and absence of water, emphasizing the significant impact of water on stress distribution within the galleries.

When the dam is full, the maximum tensile stress values at both the top gallery node 889 and the bottom gallery node 878 increased significantly, rising by 4 and 5 times, respectively, compared to the empty situation. Additionally, there was a 10% increase in tensile stresses within the galleries when compared to the empty condition. This highlights the substantial impact of the water-filled state on the tensile stresses experienced in the galleries of the dam.

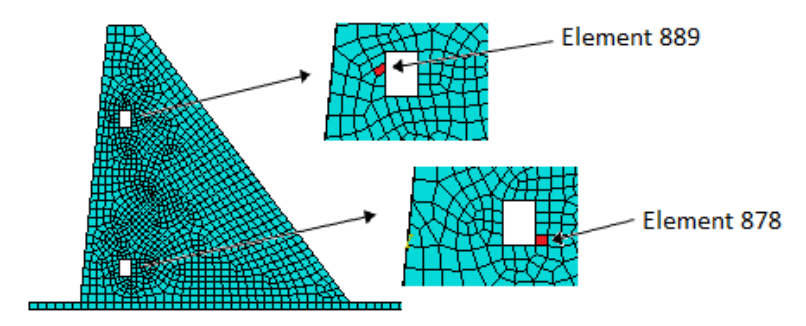
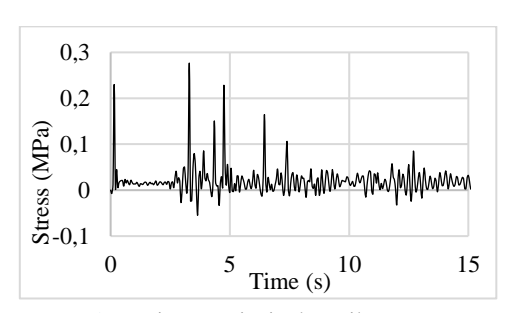
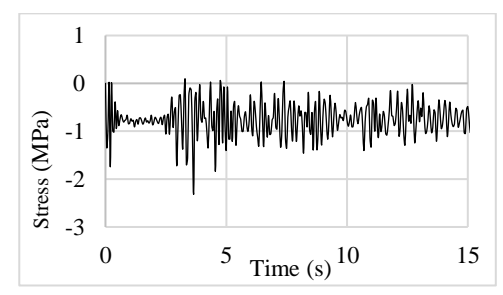


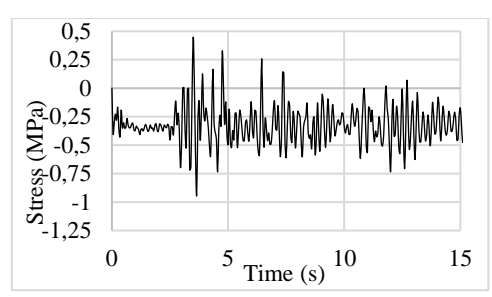
Fig. 25. Selected stress points around galleries

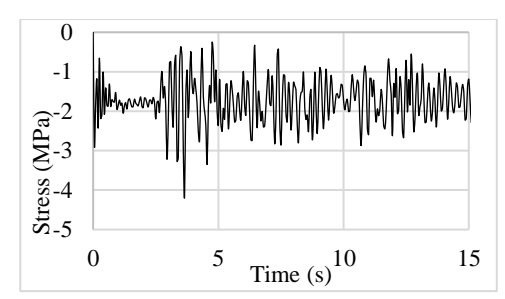




- a) Maximum principal tensile stress
- b) Maximum principal compressive stress

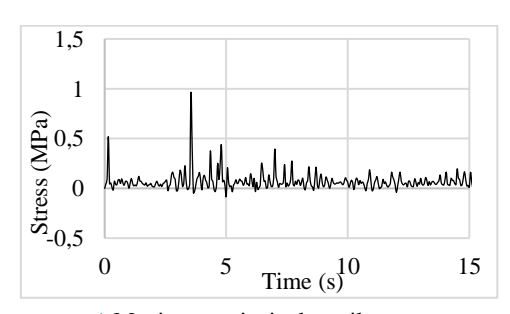
Fig. 26. Stress changing at Element 889 for empty reservoir condition during the earthquake

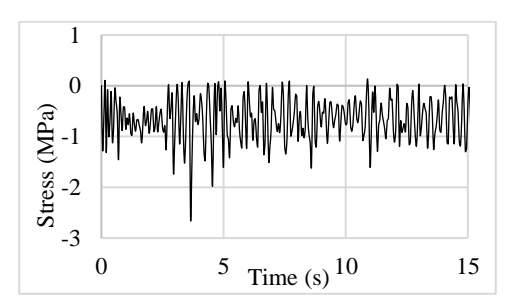




- a) Maximum principal tensile stress
- b) Maximum principal compressive stress

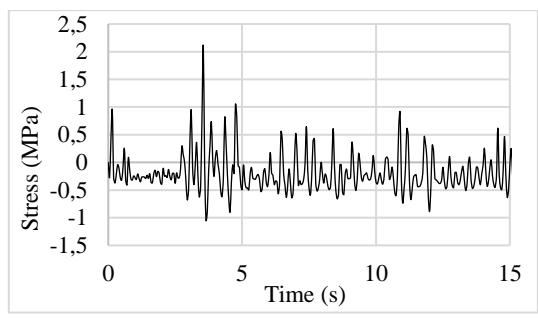
Fig. 27. Stress changing at Element 878 for empty reservoir condition during the earthquake

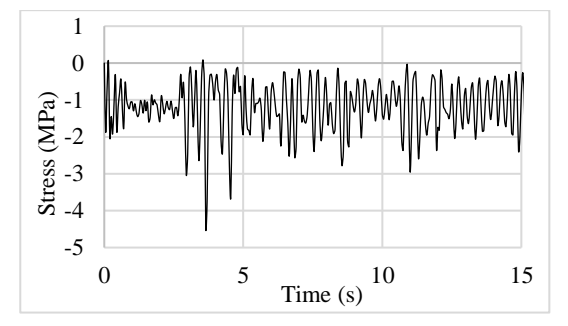




- a) Maximum principal tensile stress
- b) Maximum principal compressive stress

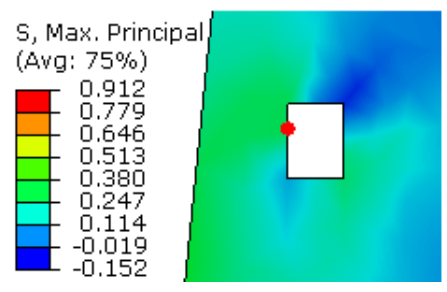
Fig. 28. Stress changing at Element 889 for full reservoir condition during the earthquake

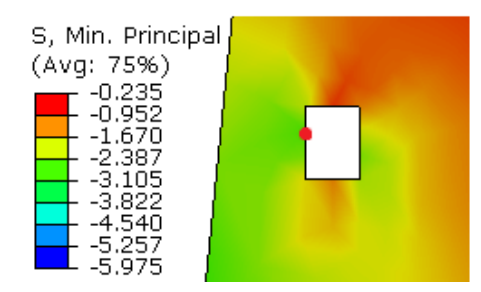




- a) Maximum principal tensile stress
- b) Maximum principal compressive stress

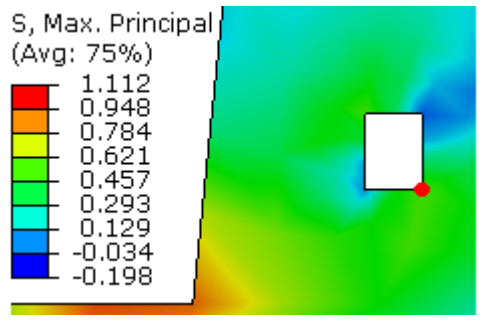
Fig. 29. Stress changing at Element 878 for full reservoir condition during the earthquake

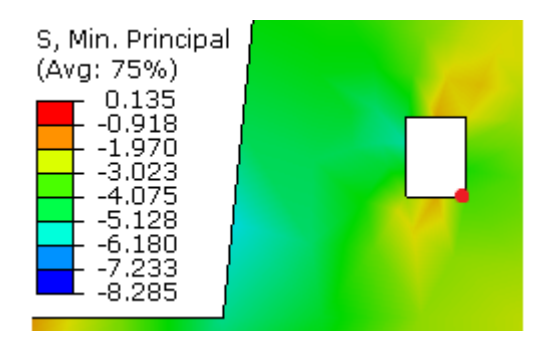




- a) t=3.30 s, max tensile stress= 0.276 MPa
- b) t= 3.65 s, min compressive stress= -2.317 MPa

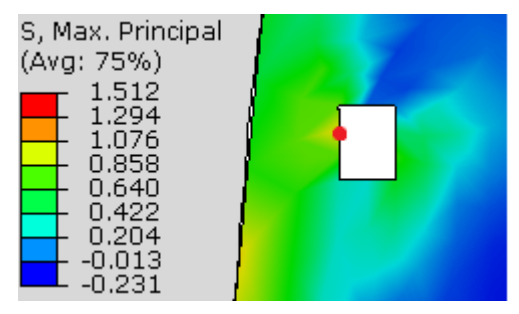
Fig. 30. Maximum and minimum principal stresses at top gallery element 889 in empty condition

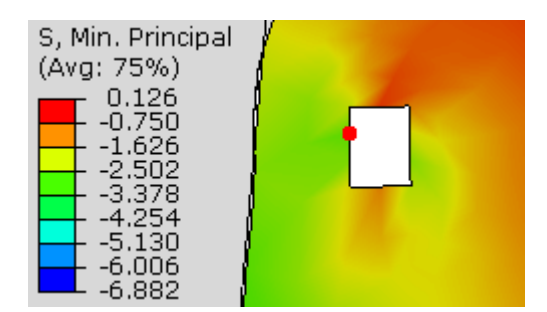




- a) t= 3.50 s, max tensile stress= 0.448 MPa
- b) t= 3.65 s, min compressive stress= -4.171 MPa

Fig. 31. Maximum and minimum principal stresses at bottom gallery element 878 in empty condition





- a) ) t= 3.55 s, max tensile stress= 0.965 MPa
- b) t= 3.65s, min compressive stress= 2.613 MPa

Fig. 32. Maximum principal stresses at top gallery element 889 in full condition

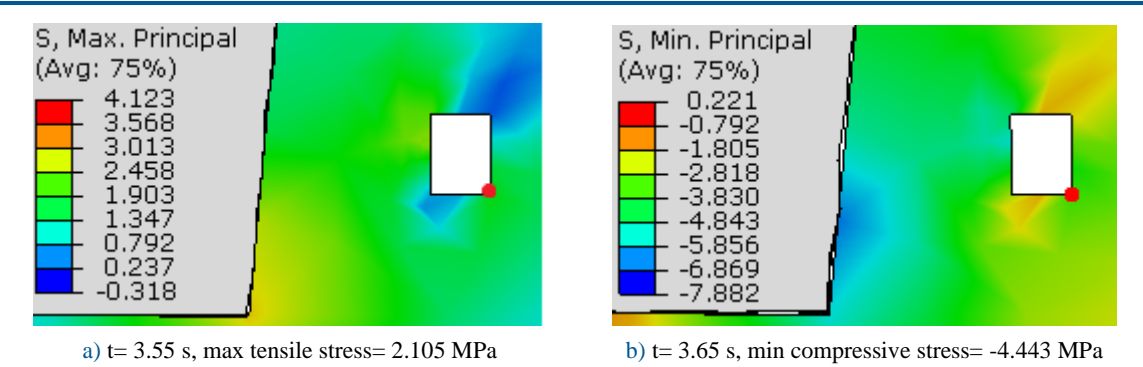


Fig. 33. Maximum principal stresses at bottom gallery element 878 in full condition

### 5. Conclusions

In this study, we investigated the effect of galleries on a selected dam's responses. Therefore, maximum principal stress components and horizontal displacements are investigated. In addition to this, the effect of the hydrodynamic pressure of the reservoir water on dam response was also examined. Elastic material behavior and geometrically linear behavior are utilized in analyses. The fixed boundary conditions and welded contact between the dam and foundation were taken into consideration in this paper. We can conclude from several results from the realized study.

- The performed numerical analyses indicate that larger principal tensile and compressive stresses
  were obtained under hydrodynamic pressure effects. The presence of reservoir water increased the
  maximum tensile stresses by approximately 215% and the compressive stresses by approximately
  10%.
- Reservoir water effects increase horizontal displacements at the crest. The presence of reservoir water increased the horizontal displacement by approximately 11% in the upstream direction and by approximately 52% in the downstream direction.
- It has been observed that sudden stress changes occur around the galleries inside the dam due to sudden discontinuity.
- Using the combined Eulerian-Lagrangian approach, it was possible to observe the turbulence and surface fluctuations of the reservoir water. Around 1.0 meters of water surge was recorded on the water surface near the crest.

According to this study, the reservoir water and the galleries within the dam body should be included in numerical models for researchers as the most critical conditions are obtained.

Beyond these results, it can be proposed that further studies may be needed to better understand the response of these types of dams. Dynamic materially non-linear analysis should be carried out to determine the earthquake performance of the dam. On the other hand, different dam-foundation interaction models can be considered and the results should be discussed in later studies. The viscous, nonreflecting, silent, or quiet boundary conditions should be taken into account to determine the more realistic response of the dam under strung ground motion effects. On the other hand, it is advised that optimum galleries' shape and geometry should be investigated for this type of dam. Three-dimensional finite element analyses of this type of dams should be considered.

#### Conflict of interests

The author(s) declared no potential conflicts of interest with respect to the research, authorship, and/or publication of this article.

### **Funding**

This research received no external funding.

### Data availability statement

Data generated during the current study are available from the corresponding author upon reasonable request.

### References

- [1] Emiroğlu ME (1998) RCC barajlarda yeni tasarım kavramları. Türkiye Mühendislik Haberleri 1998(393) (in Turkish).
- [2] Noorzaei J, Bayagoob KH, Thanoon WA, Jaafar MS (2006) Thermal and stress analysis of Kinta RCC dam. Eng. Struc. 28:1795–1802. https://doi.org/10.1016/j.engstruct.2006.03.027.
- [3] Jaafar MS, Bayagoob KH, Noorzaei J, Thanoon WA (2007) Development of finite element computer code for thermal analysis of roller compacted concrete dams. Adv. Eng. Softw. 38:886–895. <a href="https://doi.org/10.1016/j.advengsoft.2006.08.040">https://doi.org/10.1016/j.advengsoft.2006.08.040</a>.
- [4] Omidi O, Valliappan S, Lotfi V (2013) Seismic cracking of concrete gravity dams by plastic—damage model using different damping mechanisms. Finite Elem. Anal. Des. 63:80–97.
- [5] Huang H, Chen B (2012) Dam seepage monitoring model based on dynamic effect weight of reservoir water level. Energy Procedia 16:159-165. <a href="https://doi.org/10.1016/j.egypro.2012.01.027">https://doi.org/10.1016/j.egypro.2012.01.027</a>.
- [6] Araujo JM, Awruch AM (1996) An objective cracking criterion for the analysis of concrete dams. Comput. Struct. 59:751-756. https://doi.org/10.1016/0045-7949(95)00295-2.
- [7] Yilmazturk MS, Arici Y, Binici B (2015) Seismic assessment of a monolithic RCC gravity dam including three-dimensional dam–foundation–reservoir interaction. Eng. Struc. 100:137–148. <a href="https://doi.org/10.1016/j.engstruct.2015.05.041">https://doi.org/10.1016/j.engstruct.2015.05.041</a>.
- [8] Liang RY, Nusier OK, Malkawi AH (1999) A reliability-based approach for evaluating the slope stability of embankment dams. Eng. Geol. 54: 271–285. https://doi.org/10.1016/S0013-7952(99)00017-4.
- [9] Xiong K, Weng Y (2013) Seismic failure modes and seismic safety of hardfill dam. Water Sci. Eng. 6:199-214. https://doi.org/10.3882/j.issn.1674-2370.2013.02.008.
- [10] Cheng L, Zheng D (2013) The identification of a dam's modal parameters under random support excitation based on the Hankel matrix joint approximate diagonalization technique. Mech. Syst. Signal Process. 42:42–57. <a href="https://doi.org/10.1016/j.ymssp.2013.07.015">https://doi.org/10.1016/j.ymssp.2013.07.015</a>.
- [11] Zhong H, Lin G, Li X, Li J (2011) Seismic failure modeling of concrete dams considering heterogeneity of concrete. Soil Dyn. Earthq. Eng. 31:1678–1689. https://doi.org/10.1016/j.soildyn.2011.07.001.
- [12] Li M, Guo X, Shi J, Zhu Z (2015) Seepage and stress analysis of anti-seepage structures constructed with different concrete materials in an RCC gravity dam. Water Sci. Eng. 8:326–334. https://doi.org/10.1016/j.wse.2015.10.001.
- [13] Sharma V, Fujisawa K, Murakami A (2020) Space-time FEM with block-iterative algorithm for nonlinear dynamic fracture analysis of concrete gravity dam. Soil Dyn. Earthq. Eng. 131.
- [14] Wang G, Wang Y, Lu W, Yu M, Wang C (2017) Deterministic 3D seismic damage analysis of Guandi concrete gravity dam: A case study. Eng. Struc. 148:263–276.
- [15] Calayir Y, Karaton M (2005) Seismic fracture analysis of concrete gravity dams including dam–reservoir interaction. Comput. Struct. 83(19-20):1595–1606.
- [16] Bayraktar A, Türker T, Akköse M, Ateş Ş (2010) The effect of reservoir length on seismic performance of gravity dams to near- and far-fault ground motions. Nat. Hazards 52:257–275.
- [17] Kartal ME (2012) Three-dimensional earthquake analysis of roller compacted concrete dams. Nat. Hazards Earth Syst. Sci. 12(7):2369–2388.
- [18] Huang J (2018) An incrementation-adaptive multi-transmitting boundary for seismic fracture analysis of concrete gravity dams. Soil Dyn. Earthq. Eng. 110:145–158.
- [19] Kartal ME, Cavusli M, Sunbul AB (2017) Assessing seismic response of a 2D roller-compacted concrete dam under variable reservoir lengths. Arab J Geosci 10:488.

[20] Zhuo L, He JD, Xie HQ (2013) Seismic deformation and seismic resistance analysis of Shapai Roller Compacted Concrete Arch Dam based on field monitoring and dynamic finite element method. J. Mt. Sci. 10:137-148. https://doi.org/10.1007/s11629-013-2324-2.

- [21] Mejia LH, Sun JI, Leung KK (2005) Seismic upgrade of hydraulic fill dam by buttressing. Soil Dyn. Earthq. Eng. 25:571–579.
- [22] Wang G, Wang Y, Lu W, Zhou C, Chen M, Yan P (2015) XFEM-based seismic potential failure mode analysis of concrete gravity dam water—foundation systems through incremental dynamic analysis. Eng. Struc. 98:81–94
- [23] Hariri MA, Kolbadi SM, Kianoush MR (2016) FEM-based parametric analysis of a typical gravity dam considering input excitation mechanism. Eng. Geol. 84:22–43. https://doi.org/10.1016/j.enggeo.2014.05.011.
- [24] Jiang S, Du C (2012) Hazard and seismic reinforcement analysis for typical large dams following the Wenchuan earthquake. Soil Dyn. Earthq. Eng. 194: 86–97. <a href="https://doi.org/10.1016/j.soildyn.2016.01.013">https://doi.org/10.1016/j.soildyn.2016.01.013</a>.
- [25] Hariri-Ardebilia MA, Seyed-Kolbadi SM, Saouma VE, Salamon J, Rajagopalana B (2018) Random finite element method for the seismic analysis of gravity dams. Eng. Struc. 171:405–420.
- [26] URL: http://www.ce.memphis.edu/1112/notes/project\_2/beam/ACI\_mix\_design.pdf. (CIVL). Unpublished Note.
- [27] Benson DJ, Okazawa S (2004) Contact in a multi-material Eulerian finite element formulation. Comput. Methods Appl. Mech. Eng. 193:4277-4298.
- [28] Benson DJ (1997) A mixture theory for contact in multi-material Eulerian formulations. Comput. Methods Appl. Mech. Eng. 140:59-86.
- [29] Bathe K.J (1996) Finite Element Procedures. Prentice-Hall, Upper Saddle River, NJ.
- [30] Belytschko T, Liu KW, Moran B (2000) Non-linear Finite Element Analysis for Continua and Structures. Wiley, NY.
- [31] Al-Athel KS, Gadala MS (2011) Eulerian volume of solid (VOS) approach in solid mechanics and metal forming. Comput. Methods Appl. Mech. Eng. 200:2145-2159.
- [32] Wilson EL, Khalvati M (1983) Finite elements for the dynamic analysis of fluid-solid systems. Int. J. Num. Meth. Eng. 19:1657–1668.
- [33] Erdik M (2001) Report on 1999 Kocaeli and Düzce (Turkey) Earthquakes. Structural Control for Civil and Infrastructure Engineering. pp. 149-186. https://doi.org/10.1142/9789812811707\_0018.
- [34] Skrzat A (2012) Application of coupled Eulerian-Lagrangian approach in metal forming simulations. Mechanika 84 (4/12). https://doi.org/10.7862/rm.2012.9.
- [35] ABAQUS Version 6.14 (2014) ABAQUS User's Manual. Dassault Systèmes, SIMULIA.